Pergamon

PII: S0094-5765(96)00139-7

Acta Astronautica Vol. 39, No. 1–4, pp. 217–227, 1996

0094-5765/96 $15.00 + 0.00

HELIOSPHERIC LINKS EXPLORER (HELIX)

Dr. David M. Rust
The Johns Hopkins University
Applied Physics Laboratory
Johns Hopkins Road
Laurel, MD 20723-6099

Phone: (301) 953-5414
Fax: (301) 953-6670
e-mail: dave_rust@jhuapl.edu

N. U. Crooker	Boston University
R. E. Gold	The Johns Hopkins University Applied Physics Laboratory
L. Golub	Smithsonian Astrophysical Observatory
A. J. Hundhausen	High Altitude Observatory, National Center for Atmospheric Research
L. J. Lanzerotti	Bell Laboratories, Lucent Technologies
A. J. Lazarus	Massachusetts Institute of Technology
N. Seehafer	University of Potsdam
L. J. Zanetti	The Johns Hopkins University Applied Physics Laboratory
R. W. Zwickl	Space Environment Laboratory National Oceanic and Atmospheric Administration

ABSTRACT

The proposed HELIX mission will provide stereoscopic images of solar mass ejections from their origins on the Sun to their arrival at Earth. With an array of telescopes and plasma detectors, it will investigate magnetic helicity conservation in the heliosphere. Helicity conservation, which has been used successfully to describe the behavior of plasmas in fusion experiments, may explain why there are solar ejections and how they evolve in interplanetary space. HELIX uses two identical spacecraft in heliocentric ecliptic orbits. One remains near Earth and the other drifts so that it will see solar features up to five days before they are visible from Earth. This will provide advance warning of areas on the Sun that can provide geomagnetic storms at Earth.

SCIENCE INVESTIGATION

The scientific objectives of the HELIX mission can be summarized in three lines:

- Track eruptions from the Sun's surface to Earth's orbit
- Test magnetic helicity conservation
- Develop geomagnetic storm forecast techniques

By achieving these goals we will greatly advance understanding of the most common form of matter in the universe: magnetized plasma. In the process we will determine the origin of the disturbances that pummel our Earth's magnetosphere and so severely disrupt modern space and technological systems.

The HELIX mission is motivated by recent theoretical insights into coiled magnetic fields and by the development of instruments that, for the first time, will allow solar eruptions to be tracked in fine detail from their onset to their impact with Earth.

Solar Ejections

Coronal mass ejections (CMEs) are bright features that move outward through the million-degree solar corona at speeds from 10 to 2000 km s^{-1}. The heart of many mass ejections is a twisted, filamentary structure marked by cool material that was previously a solar prominence. The spectacular nature of the largest mass ejections is illustrated in Figure 1 by images

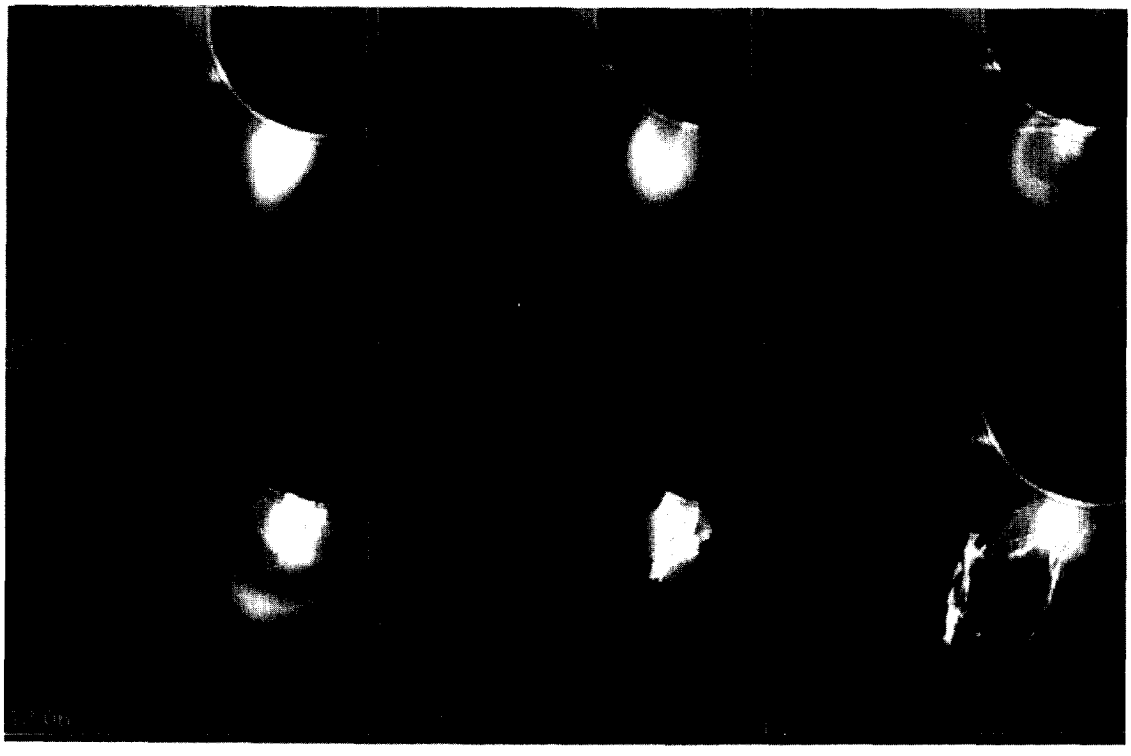

Figure 1. A CME and erupting solar prominence on August 18, *1980. The distribution of helicity in this event was analyzed by* House and Berger [1987].

obtained in August 1980, with the coronagraph on the SMM spacecraft. The spatial scales, mass motions, and energies involved in this phenomenon are larger than those in any other form of solar activity.

Explaining the sudden expulsion of a highly conducting plasma from the magnetized Sun presents a major, so-far unanswered, challenge. The striking effects of mass ejections and other solar wind disturbances on planetary magnetospheres, comets, and cosmic rays provide even more motivation and extend the significance of mass ejections well beyond the traditional realm of solar physics.

Magnetic Helicity

There are only two long range forces of consequence in astrophysical contexts: gravity and electromagnetism. The study of solar magnetism has been a leading catalyst for extending knowledge about magnetic fields in the cosmos generally. Magnetic fields in astrophysical settings are filamentary and tend to concentrate in bundles, called magnetic flux ropes. Such ropes are best known from solar observations.

The law of conservation of magnetic flux Φ is fundamental to understanding the behavior of magnetic flux ropes in highly conducting plasmas (Alfvén's frozen-flux theorem). The law tells us that Φ in such a plasma does not decay with time and the only way it can change at a particular location in space is when the plasma carrying the flux itself moves, dragging the flux with it. It is impossible to underestimate the importance of this law as no physical understanding of the behavior of magnetic flux ropes can be achieved without it.

There is another conservation law for magnetic fields which is possibly of no less importance. This is the law of conservation of magnetic helicity. Helicity conservation restricts the form of the lowest energy state that a magnetic configuration can take to the force-free state.

This fact was successfully used by Taylor[1] to describe relaxation in laboratory plasmas. But in space physics, conservation of magnetic helicity has not been used as widely. Magnetic helicity H_m is defined as

$$H_m = \int_V \mathbf{A} \bullet \mathbf{B} dV, \qquad (1)$$

where **A** is the magnetic vector potential. To formulate magnetic helicity as a physical quantity, a suitable choice of boundary conditions is needed to make it gauge independent. This dependence on boundary conditions makes magnetic helicity a global (topological), instead of a local, quantity. But with suitable specification of gauge and boundary conditions, H_m can be specified in variables that can be measured. For example, the magnetic helicity of a twisted flux rope is $T\Phi^2$ where T is the total twist in radians.

A helicity-conserving flux-rope model[2] seems to explain the average thermodynamic and magnetic properties of interplanetary magnetic clouds. But helicity conservation holds strictly only in ideal magnetohydrodynamics, where conductivity is infinite. Confirmation that magnetic helicity is conserved in interplanetary magnetic clouds will encourage extension of the principle to a wide range of astrophysical contexts and, we believe, make a fundamental contribution to science comparable to Alfvén's frozen-flux theorem. It should allow accurate predictions of the energy and field configuration in magnetic clouds to be made on the basis of solar data obtained with HELIX telescopes. What is needed is a means of determining the sense of twist (right-handed or left-handed) as well as 3-D images (to determine the pitch) and measurements of the underlying magnetic fields.

Helicity and the Solar Dynamo

All forms of solar activity owe their existence to the solar dynamo which works below the visible surface of the Sun. Two parts constitute the solar dynamo field: the toroidal (azimuthal) field, which is strong, and the weak poloidal field (with field lines in planes containing the rotational axis of the Sun). According to standard dynamo theory, the toroidal field is easily generated from the poloidal one by the differential rotation of the Sun. The regeneration of the poloidal field from the toroidal one is much more complicated and thought to be accomplished by the alpha effect, namely the generation of a mean electromotive force (emf) along a mean, or large-scale, magnetic field by turbulently fluctuating, or small-scale, parts of velocity and magnetic field.

The alpha effect represents the central mechanism in the kinematic theory of the turbulent dynamo. In the framework of this theory, the presence of kinetic and magnetic helicities facilitates a dynamo effect.[3]

Since helicities cannot be measured directly in the solar convection zone, it will be very helpful to measure them in the atmosphere and in the solar wind. For instance, there is strong observational evidence that the helicity of active regions is predominantly negative in the northern and positive in the southern hemisphere.[4, 5, 6]

In order to discriminate among alternative theoretical explanations of this, and to achieve a satisfactory dynamo model, we must determine the latitude variation of helicity emergence and ejection. A powerful way to accomplish this is to measure the size and twist in ejecta. With its full-sky coverage, HELIX will help to measure the helicity density of all solar wind plasmas and so establish the amount of helicity generated and the routes of escape.

Geomagnetic Storms

Fast CMEs are believed to be the direct cause of the largest geomagnetic storms,[7, 8] independent of whether they are recurrent or nonrecurrent.[9] Fast CMEs are preceded by shocks that cause sudden storm commencements, and they bring strong magnetic fields with substantial north-south components both in the postshock flow and within the CME itself. Years of research in magnetospheric physics have demonstrated that a strongly southward interplanetary magnetic field component is essential to the creation of a large geomagnetic storm. Thus, predicting the magnetic field orientation and the speed of

CMEs is central to predicting geomagnetic storms.

Based on what we now know about the global helicity pattern in the Sun's magnetic fields, we can predict that the pattern of magnetic field orientations within most magnetic clouds should be a simple function of solar cycle number: i.e. the field in a magnetic cloud, as seen by an observer at 1 AU, should rotate southward, then northward, during even-numbered solar cycles, but northward, then southward, during odd solar cycles.

We will use the planned observations of the HELIX satellites to test this hypothesis and thereby improve our ability to predict geomagnetic activity. During odd solar cycles, strongly southward IMF should occur at the leading edge of a solar wind cloud, shortly after shock passage. Under these conditions, a storm will immediately follow an SSC (Sudden Storm Commencement). The approaching cycle is number 23, so most geomagnetic storms caused by magnetic clouds should start with very little warning after an SSC. The characteristics of storms not caused by magnetic clouds may still be influenced by the distribution of magnetic flux and helicity in streamer belts.

TECHNICAL APPROACH

Mission Description

HELIX uses two identical spacecraft, HELIX-1 and HELIX-2, in heliocentric ecliptic orbits approximately 1 AU from the Sun. The two spacecraft drift away from Earth at different rates. The HELIX-1 and HELIX-2 trajectories are shown in Figure 2 in a rotating ecliptic-plane plot with fixed Sun-Earth line.

HELIX-2 has a period of 397 days. Due to its angular rate of motion around the Sun, it drifts away from Earth at a rate of 30° per year. After two years it will be approximately 1 AU from Earth.

HELIX-1 remains close to Earth, but in a heliocentric orbit. This avoids eclipses and yields viewing angles of the Earth and Sun similar to those of HELIX-2, allowing identical spacecraft

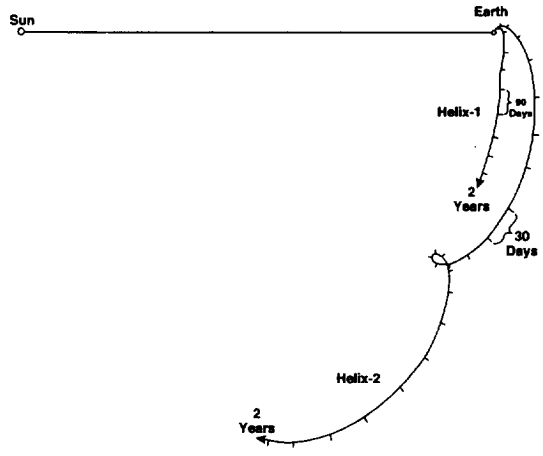

Figure 2. Angular separation of the HELIX spacecraft as the mission progresses allows tomographical observations of solar disturbances.

design. Due to the dynamics of the Sun-Earth-spacecraft three-body system, the drift rate for HELIX-1 cannot be arbitrarily small without looping around the L2 libration point. To avoid such orbits, the ejection of HELIX- 1 from Earth's gravitational sphere of influence causes a drift rate of about 10° per year, one-third that of HELIX-2.

Launch and Injection

The spacecraft are launched into a phasing Earth orbit with a period of ten days, a C_3 of -1.6 km^2/s^2, and an apogee slightly beyond the Moon's orbit. Lunar gravity assist is utilized to eject the spacecraft from Earth orbit, an approach used successfully by Wind, Geotail, and Clementine. Two to four revolutions are completed in the phasing orbit before encountering the Moon, allowing plenty of time for correction maneuvers to achieve optimum placement. A lunar swingby, at 4 to 6 lunar radii, achieves the desired heliocentric orbits; these are higher energy and longer period orbits compared to Earth's orbit.

Data Acquisition

HELIX spacecraft acquire, process, store and downlink images and measurements of the interplanetary plasmas eight times daily for the duration of the two-year mission.

A simple, repetitive data acquisition and downlinking process maximizes the use of data link capacities as the two spacecraft move away from Earth. Data acquisition and downlink operations use a 3-h cycle. During the first two hours, the instruments continuously acquire data during two rotations of the spacecraft. The third hour is dedicated to downlink. To achieve high downlink data rates with low resource cost, an X-band link using the 34-m beam waveguide DSN antenna is assumed.

For the first few months, both spacecraft are able to downlink the maximum 2 Gbits of storage within the allocated l-h period.

During the third month, the HELIX-2 spacecraft lowers its downlink data rate to maintain link margin, dropping its data rate and volume to 500 kbps and 1.8 Gbits per dump respectively. As the mission continues, the HELIX-2 spacecraft decreases its data rate to accommodate the link capacity, ending up at 7.8 kbps and 28 Mbits per dump after 2 y.

The HELIX- 1 spacecraft remains at full downlink rate until ~ 8 mo into the mission. From then on, the data rate slowly decreases to 62.5 kbps and 225 Mbits per dump.

INSTRUMENTATION

Each HELIX spacecraft carries a payload of four instruments:

Helium Doppler Imager (HDI)
Tomographic Imaging Polarimeter (TIP)
Solar Wind System (SWS)
Magnetometer (MAG)

Helium Doppler Imager (HID)

The HID instrument provides simultaneous high resolution images and velocity maps of chromospheric eruptions in the 304 Å He II line.

The expected velocity resolution with 1% photometry is 45 km/s. With 2.5 arcsec pixels and a 1.4° field-of-view (FOV), the HDI will be able to monitor the eruption of filaments, prominences, and the early evolution of CME's.

Operating with a 15-s cadence, HDI will obtain more than 90 image pairs of a CME moving at 1000 km/s. The combination of stereoscopic intensity and velocity data and rapid cadence and time resolution will provide constraints on models of instabilities that give rise to the eruptions.

The HDI uses a set of multilayer coated optics with two selectable light paths focused onto a single large-format CCD camera (Fig. 3). Imaging is provided by a 6-cm diameter f/20 off-axis paraboloid mirror, and Doppler-shift information is provided by the two flat-feed mirrors selected by a shutter.

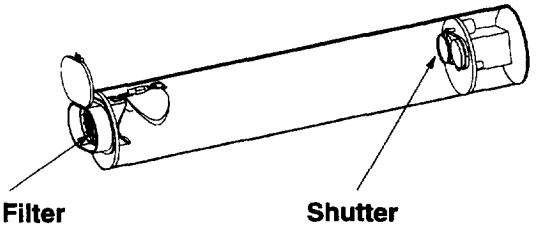

Figure 3. The two HDI telescopes produce high-resolution intensity and velocity images.

The focusing optic is fed alternately by either of two flat mirrors. The focus mirror is tuned to precisely the He II 304 Å wavelength, and the two flat mirrors are tuned above and below 304 Å, such that the strong gradient in the multilayer response curve is positioned at 304 Å. The effect of this arrangement is to provide a sensitive measurement of Doppler shifts while simultaneously giving high-quality imaging at the unshifted wavelength. Material moving toward or away from the observer will be brighter or fainter than average, depending upon the slope of the multilayer response. Thus, the difference image is a dopplergram and the sum of the two images is an on-band image.

An aluminum pre-filter at the entrance aperture prevents solar heat and UV radiation from reaching the optics, and also provides the first stage of visible-light reduction. A factor of 10^{10} rejection is achieved for visible light with a second aluminum filter placed directly in front of the camera.

The CCD is made sensitive to XUV photons by overcoating with a thin (0.4 μm) layer of

Lumigen. The format of the CCD is 2K x 2K, with 15 μm pixels. It operates with moderate cooling at -40C. The shutter is closed during readouts to avoid smearing the image. Because full-resolution images are not always needed, the camera can be read out using $n \times m$ pixel binning, or it can be windowed for partial field readout.

Tomographic Imaging Polarimeter (TIP)

Imaging solar mass ejections from beyond the range limit of coronagraphs out to >1 AU requires an instrument that scans the full sunward hemisphere from elongation angles of ~20° to beyond 90°. Near the Sun, CMEs are relatively bright compared to the dark sky, but the suppression of scattered sunlight is crucial to obtaining a good image. As the CME moves outward, its density drops and the intensity of light Thomson-scattered from the electrons is reduced, approximately as R^{-4}. We have designed the TIP to record CMEs and other disturbances over a very wide angular range and correspondingly wide dynamic range. Polarization measurements will allow determination of the distance between the spacecraft and various cloud elements along the line of sight.

Previous attempts to reconstruct CME densities from two views[10, 11, 12, 13] were made with non-simultaneous views nearly 90° apart. In these analyses, tests of an iterative least-squares tomography technique showed that when density structures are simple, such as a hollow sphere or two adjacent spheres,[13] tomography can reproduce them, but restrictive and perhaps unrealistic assumptions about the outward motion and expansion of observed structures were required. No such assumptions are necessary when simultaneous views from two angles are available. Polarization data will be used to separate near voxels (volume elements) from far ones.

TIP images will be about 200 x 200 pixels. We plan to use a standard row-action type inversion, such as the SIRT[14] algorithm to deconvolve them.

The TIP images CMEs by scanning the heliosphere for enhancements in the dark sky background. Each of the instrument's three heads has a field-of-view of 30° x 1° for each of three polarization states. These sensors are combined to form a 90° x 3° composite FOV, which allows CMEs to be tracked from elongation angles of 20° to 110°. Rotation of the spacecraft (Fig. 4) sweeps the FOV around the Sun, providing full-sky coverage in the area of interest.

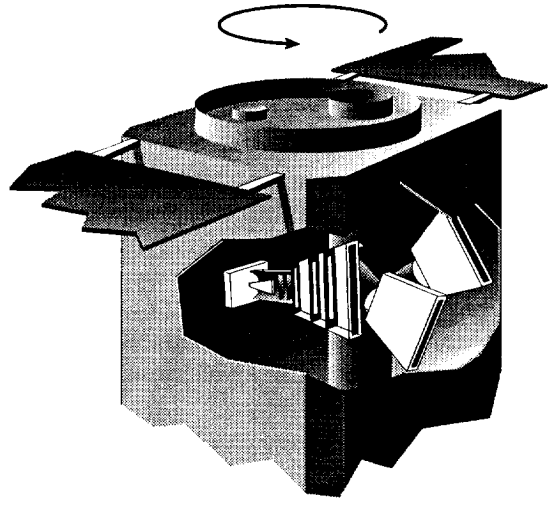

Figure 4. TIP sensors (white) scan a hemisphere during each spacecraft rotation.

The TIP CCD pixel FOV is 0.092° x 0.055°. Pixels are summed to an intermediate super-pixel for transmission to the ground. A full hemisphere image is assembled from individual super-pixels by first eliminating those that contain bright stars and then summing groups of adjoining pixels. Successive images of the dark sky, which is dominated by the zodiacal light and faint stars, are then subtracted on the ground to bring out the small-scale structure and extent of transient enhancements.

TIP's three cameras operate asynchronously in one parameter-driven operating mode. As the spacecraft rotates, the TIP cameras continuously acquire images at 3-s intervals; during each integration period, three polarization state images are obtained simultaneously. Long integration intervals are desirable to maximize signal-to-noise ratio and simultaneously reduce

telemetry requirements. Time-delay integration is employed on the CCD to eliminate pixel smearing; CCD pixel rows are shifted at appropriate intervals during integration to compensate for the rotation.

Baffle/Cover Mechanism. The baffle design (Fig. 5) ensures that scattered light from the Sun is well below CME signal levels. A two-stage baffle system prevents direct sunlight from falling onto the aperture. No illuminated edge is seen by the entrance aperture. The first edge prevents any direct sunlight from entering the baffle, and the second stage prevents the optics from seeing the illuminated edge of the first stage. Theoretical diffraction predictions have been confirmed with measurements of prototype

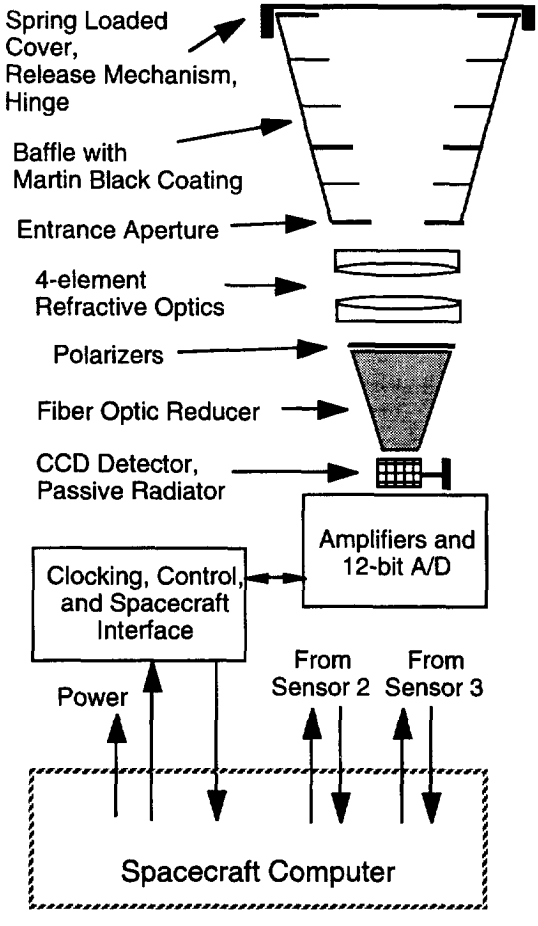

Figure 5. The TIP produces low noise CME images.

baffles. The first edge gives an intensity reduction of 3×10^{-5}. The second edge has to diffract the light by 15° for it to reach the lens. This causes a further reduction of approximately 10^{-5} to give a total attenuation of about 3×10^{-10}. Further attenuation depends on the low Bidirectional Reflectance Distribution Function (BRDF) of the optics. For the energy to enter the detector it has to be scattered by the optics through about 4°. A conservative estimate of the BRDF of the lens at this angle is 10^{-2} sr^{-1}. The FOV of the optics subtended at the baffle is 10^{-3} so the reduction due to the BRDF is 10^{-5}. The total attenuation becomes 3×10^{-15}, and scattered light does not significantly contribute to the noise function.

Since the signal from Thomson scattering is small compared to background sources, signal to-noise analysis is of paramount importance. Calculations indicate that S/N ratios of 75 are obtained for 1 deg^2 pixels at 20° elongation. The S/N decreases as elongation increases, reaching a value of 4 for 2.5 deg^2 pixels at 110° elongation.

Solar Wind System (SWS)

While the TIP provides remote imaging to identify CMEs, *in-situ* measurements will be essential to identify and quantify the southward swings of the magnetic field and the increases in solar wind ram pressure believed to cause geomagnetic responses. Two-point measurements from the planned SWS instruments will help characterize the spatial extent, structure and rate of expansion of the driving CME and associated shocks (for fast CMEs).

Solar wind particle spectra are obtained using two Faraday cup sensors. The SWS ion sensor has its FOV centered on the Sun and provides proton and alpha-particle parameters. It uses a circular collector plate split into three, 120° sectors that determine the flow direction of the ions as it continuously faces the Sun. Electron parameters are provided by a Faraday cup looking out at right angles to the Sun-spacecraft line. It will detect bidirectional electron streaming as an indicator of CMEs or other closed field line structures.

The electron sensor has a 45° half-angle, conical field of view, as does the Sun-facing ion sensor.

The energy ranges are 200 to 8 KV (ions) and 30 to 1 KV (electrons).

Figure 6 shows a schematic cross section of a Faraday Cup sensor. It contains a series of planar wire-mesh grids and one or more collector plates. The velocity distribution function of ions or electrons is measured by applying a sequence of voltages to the "modulator" grid. As illustrated in Figure 6, voltage V_1 is applied to the grid, and only particles having energy/charge, E/Q, greater than V_1 will be able to pass through the grid and continue on to strike the collector plate; a measurable current is thus produced on the plate.

In normal operation, the grid voltage is varied between two voltages, V_1 and V_2, at a frequency of a few hundred Hz. Thus, particles normally incident on the grid and having E/Q between V_1 and V_2 produce a current on the collector plate that varies at the modulation frequency and can be detected with an appropriate phase sensitive measurement system. By choosing an increasing sequence of voltages, e.g. V_2 and V_3, the E/Q spectrum of the particles can be explored.

The modulator grid voltage discriminates on the basis of the particle's velocity normal to the plane of the grid (its parallel component is unaffected). When two voltages are applied as

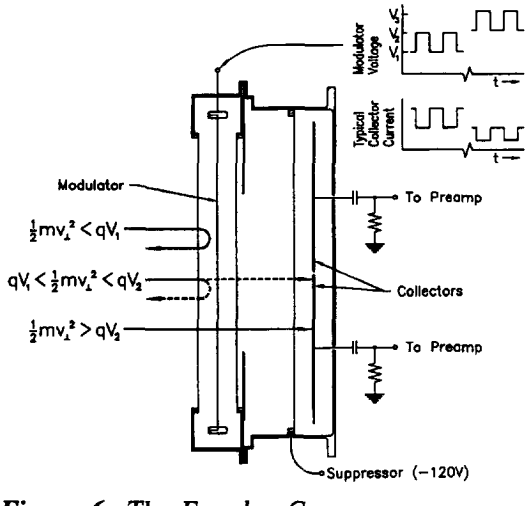

Figure 6. *The Faraday Cup sensor measures the velocity distribution function of ions or electrons.*

described above, the modulated-grid Faraday Cup sensor will define two planes in velocity space that are parallel to the sensor's energy-determining grid. It will measure currents due to particles in the plasma velocity distribution function between those two planes that are in the sensor's field of view.

Magnetometer (MAG)

The solar wind magnetic field is 1-5 nT during quiet conditions with up to an order of magnitude increase during active periods. The accuracy of the planned 3-axis vector MAG is 0.2 nT. Vector accuracy is 2°. With 16-bit digitization, it will provide pico-Tesla resolution of fine scale gradients, structure and wave phenomena. The time resolution will be 0.1 s. This time resolution corresponds to a spatial resolution of ~50 km.

On the microscale (< 60 s), MAG observations will determine the internal structure of various discontinuities, including those that bound CMEs and flux ropes. In conjunction with plasma measurements, MAG observations will enable us to distinguish between tangential and rotational discontinuities.

Observations on the macroscale will determine the spatial extent of solar wind features transverse to the Earth-Sun line. We can use the HELIX satellite pair, and the fact that their separation increases with time during the initial stage of the mission, to determine the spatial scale lengths associated with the full range of solar wind features from smallest to largest.

The variable spatial scale vector magnetic field measurements could test conservation of helicity within CMEs as they expand beyond Earth's orbit. *In situ* measurements of the apparent time sequence of magnetic fields imposed upon the Earth's magnetosphere could be input to prediction algorithms of geomagnetic activity.

MAG includes a low-noise three-axis fluxgate magnetometer for vector sampling of the DC field. A bandpass filtered AC event detection channel is also provided. Active current cancellation on the outer circuit loops of the solar panels removes magnetic interference.

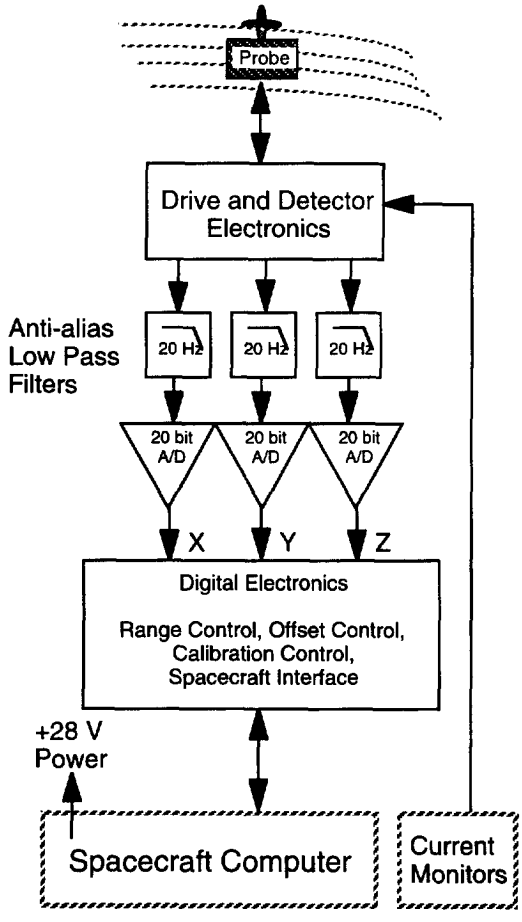

Figure 7. *The ring-core fluxgate magnetometer design features high relative accuracy and sensitivity.*

The MAG is a ring core flux gate magnetometer (Fig. 7). The sensor element is essentially used as a null detector in a feedback loop where the current required to null the field at the sensor is a measure of the field strength. The ring core geometry exhibits superior long-term zero-level stability and has minimal drive power requirements. The zero-offset stability is better than +0.1 nT over a temperature range of + 60°C for periods exceeding one year. This is commensurate with the typical spacecraft field at the sensor location and exceeds our measurement requirement of 0.2 nT.

Each of the four channels is followed by 20 Hz anti-aliasing filters and 20-bit A/D converters. Digital logic controls data collection and communications with the spacecraft computer. Processing in the spacecraft computer provides noise rejection, 5-Hz anti-alias filtering, and digital bandpass filtering on the AC channel.

Spacecraft

Table 1 summarizes the spacecraft design requirements and Figure 8 shows the spacecraft in the on-station configuration. Figure 9 shows two spacecraft can be launched together in a med-lite launch vehicle.

Table 1. Spacecraft Requirements

Interface:	Clamp-band interface consistent with Med-Lite launch vehicle capability
Power:	200 W continuous avg. 250 W peak (each spacecraft)
Mass:	300 kg (each spacecraft)
Data Rates:	7.8 - 1000 kbps)
Data Storage:	2 Gbits
Pointing Knowledge:	0.025° 3σ
Pointing Control:	0.25° 3σ
Propulsion:	100 m/s total ΔV
Radiation Tolerance:	15 krads (Si) Total Dose

Most HELIX subsystems are circuit cards using a VME-compatible backplane and a common form factor.

Received commands are processed by the command decoder, which includes watchdog timers and a hard-wired decoder for critical commands such as processor reset. These commands are forwarded to the spacecraft processor, which stores and executes time-tagged commands. The same processor performs attitude determination and control as well as instrument command processing and science data handling.

Science data are stored in a solid-state, 2-Gbit data recorder. An instrument interface between the processor and the four instruments buffers and conditions instrument commands and data and handles limited analog telemetry.

Commands are received via the high-gain antenna for normal deep-space operations or via one

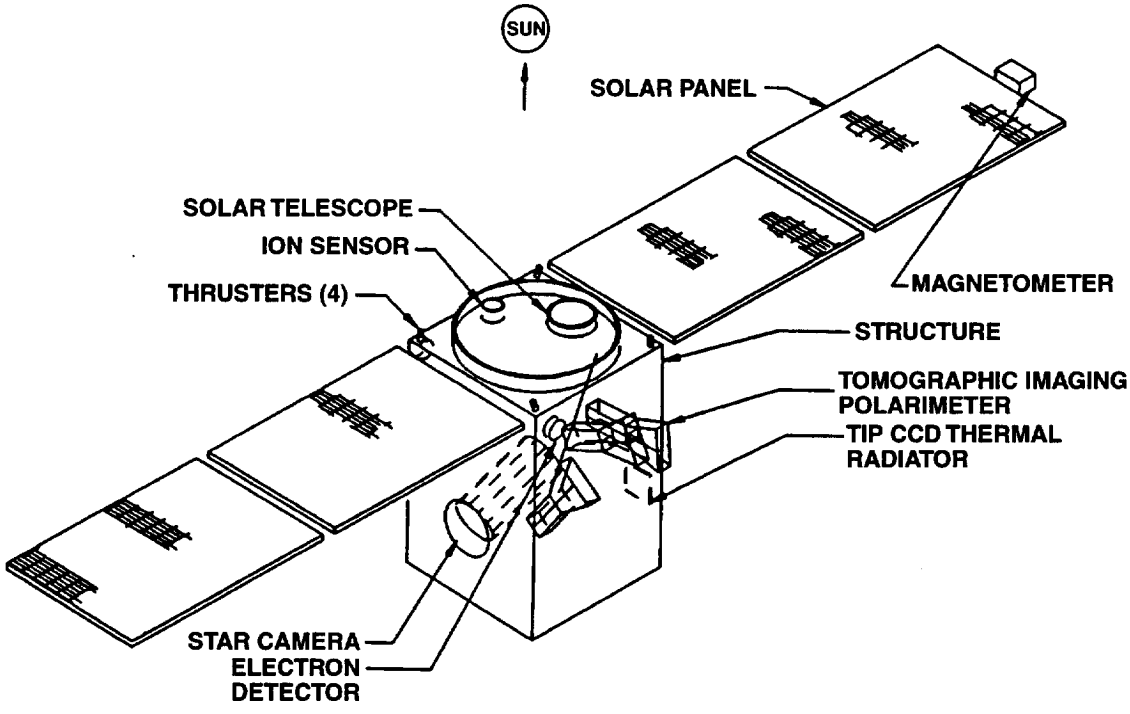

Figure 8. The on-station configuration of the HELIX spacecraft provides continuous power and required viewing angles for instruments.

of the low-gain antennas for near-Earth and emergency operations. Downlink rates will range from 1 Mbit/s in the first several months of the mission to 7.8 Kbit/s for HELIX-2 near mission end.

Attitude Determination and Control

The HELIX attitude determination and control system is a full three-axis system, although the spacecraft spends most of its time spinning with its axis pointing at the Sun. The HDI is pointed at the Sun, and the solar panels are fully illuminated while the TIP scans the full sky once each hour. The low annular rotation rates are measured by a gyro; reaction wheels are used to achieve control. Attitude determination is provided by a star camera to an accuracy of ±20 arcsec. Attitude data from the star camera and gyro, as well as wheel rates, are sent to the computer via the attitude interface card for processing. Excess wheel momentum is dumped using the hydrazine thrusters. Due to the balanced configuration and the low external torque environment, momentum dumping is expected to be minimal. Once every 3-h, the

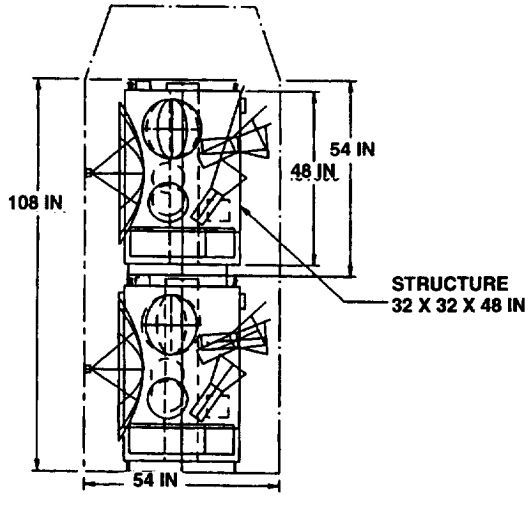

Figure 9. Two HELIX spacecraft fit in the launch vehicle dynamic envelope.

spacecraft spin will be stopped and the wheels will point the high-gain antenna at Earth for downlink. Following downlink, the spacecraft will resume Sun-pointing and restart its slow roll.

CONCLUSION

The Heliospheric Links Explorer will provide stereoscopic images of solar mass ejections from their origins on the Sun to their interaction with Earth. It will test the range of validity of helicity conservation and it will test other hypotheses about the sequence of events leading to magnetic storms. HELIX data and results would be available on the Internet where images of developing space storms could become as familiar and maybe as useful, as satellite images of tropospheric storms.

The research outlined in this paper will be essential for understanding and forecasting the effects of space weather on commercial and government enterprises, so industry has been involved from the initial concept. Industries concerned most directly with space weather include telecommunications and electrical power generation and distribution. These industries can encounter serious system problems and outages, resulting in multi-million dollar losses in equipment and services.[15]

References

[1]Taylor, J. B., Relaxation and magnetic reconnection in plasmas, *Rev. Modern Phys., 58,* 741, 1986.

[2]Kumar, A. and D. M. Rust, Interplanetary magnetic clouds, helicity conservation, and current-core flux ropes, *J. Geophys. Res.,* (in press) 1996.

[3]Seehafer, N., Current helicity and the turbulent electromotive force, *Europhys. Lett., 27,* 353-357, 1994.

[4]Seehafer, N., Electric current helicity in the solar atmosphere, *Solar Phys., 125,* 219-232, 1990.

[5]Rust, D. M., Spawning and shedding helical magnetic fields in the solar atmosphere, *Geophys. Res. Lett., 21,* 241-244, 1994.

[6]Pevtsov, A. A., R. C. Canfield, and T. R. Metcalf, Latitudinal variation of helicity of photospheric magnetic fields, *Astrophys. J., 440,* L109-L112, 1995.

[7]Gosling, J. T., S. J. Bame, D. J. McComas, and J. L. Phillips, Coronal mass ejections and large geomagnetic storms, *Geophys. Res. Lett., 17,* 901-904, 1990.

[8]Tsurutani, B. T., W. D. Gonzalez, F. Tang, and Y. T. Lee, Great geomagnetic storms, *Geophys. Res. Lett., 19,* 73-76, 1992.

[9]Crooker, N. U. and E. W. Cliver, Postmodern view of M-regions, *J. Geophys. Res., 99,* 23383-23390, 1994.

[10]Jackson, B. V., R. A. Howard, N. R. Sheeley, Jr., D. J. Michels, and M. J. Koomen, and R. M. E. Illing, Helios spacecraft and Earth perspective observations of three looplike solar mass ejection transients, *J. Geophys. Res., 90,* 5075-5081, 1985.

[11]Jackson, B. V., B. Rompolt, and Z. Svestka, Solar and interplanetary observations of the mass ejection on 7 May, 1979, *Solar Phys., 115,* 327, 1988.

[12]Jackson, B. V., *Adv. Space Res., 9,* 69, 1989.

[13]Jackson, B. V. and H. R. Froehling, Three-dimensional reconstruction of a coronal mass ejection, *Astronomy and Astrophysics, 299, 3,* 885, 1995.

[14]Olson, A. H., A chebyshev condition to accelerating convergence of iterative tomographic methods – solving large least squares problems, *Phy. Earth and Planet. Inter. 47,* 333, 1987.

[15]Lanzerotti, L. J., Impacts of solar-terrestrial processes on technological systems, D. N. Baker, V. O. Papitashvili, and M. J. Teague (eds.), *Solar Terrestrial Energy Program, COSPAR Colloquia Series,* 5, Pergamon Press, 547-555, 1994.